Matter

CellPress

Article

A high-accuracy, real-time, intelligent material perception system with a machine-learning-motivated pressure-sensitive electronic skin

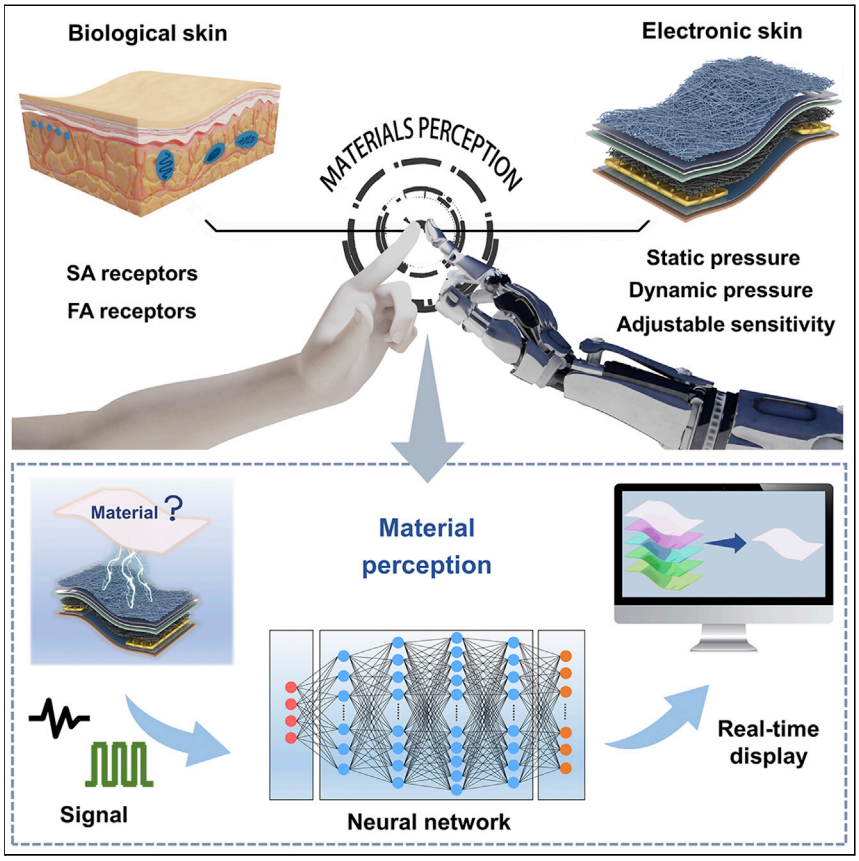

A hybrid e-skin (PTES) consisting of a triboelectric nanogenerator and a piezoresistive pressure sensor is reported, which can perceive static and dynamic tactile information with high sensitivity. The functional layers of PTES are formed by cost-effective and eco-friendly eggshell membranes in combination with a facile infiltration method. By integrating the PTES with a high-speed data collector and machine-learning technique, an intelligent material perception system that can recognize 12 materials in real time via one touch is established.

Demonstrate
Proof-of-concept of performance with intended application/response

Xiao Wei, Hao Li, Wenjing Yue, Song Gao, Zhenxiang Chen, Yang Li, Guozhen Shen

sunny_lee2011@hotmail.com (Y.L.)
gzshen@semi.ac.cn (G.S.)

Highlights

A hybrid e-skin to perceive static and dynamic tactile information

Biofilms and a simple infiltration method to realize hybrid e-skin

Piezoresistive pressure sensor with ultra-high and linearly adjustable sensitivity

Combining machine-learning techniques to realize intelligent material perception

Wei et al., Matter 5, 1–21
May 4, 2022
https://doi.org/10.1016/j.matt.2022.02.016

Please cite this article in press as: Wei et al., A high-accuracy, real-time, intelligent material perception system with a machine-learning-motivated pressure-sensitive electronic skin, Matter (2022), https://doi.org/10.1016/j.matt.2022.02.016

Matter

CellPress

Article

A high-accuracy, real-time, intelligent material perception system with a machine-learning-motivated pressure-sensitive electronic skin

Xiao Wei,[1,4] Hao Li,[1,4] Wenjing Yue,[1,2,4] Song Gao,[1,2] Zhenxiang Chen,[1,2] Yang Li,[1,2,3,*] and Guozhen Shen[3,5,*]

SUMMARY

Developing e-skins that can perceive stimuli with high sensitivity and material recognition functionality at low cost is of great importance to intelligent perception. Here, a hybrid e-skin (PTES) consisting of a triboelectric nanogenerator in tandem with a piezoresistive pressure sensor (PPS) is reported by using an eggshell membrane and infiltration method, which effectively perceives static and dynamic tactile information, such as human physiological information, manipulator tactile sensation, and human walking state. By integrating PTES with a high-speed data collector and machine learning, a material perception system capable of recognizing 12 materials in real time within one touch is established. A PTES array that can detect material property and location further demonstrates the feasibility of simultaneously processing multidimensional information. Additionally, by paralleling with a thin-film resistor, the PPS achieves an ultra-high sensitivity that can also be linearly adjusted. This PTES can open a new avenue for practical intelligent perception and realization of prominent applications.

INTRODUCTION

Electronic skin (e-skin) refers to a flexible electronic device that is able to convert external stimuli into detectable electrical signals. Owing to its salient merits of high sensitivity, wearable characteristics, and mechanical flexibility, e-skin has received a burgeoning amount of interest in areas ranging from wearable human health monitoring[1–5] to smart prosthetics[6–10] and human-machine interaction.[11–15] Inspired by the microstructures and functions of the human skin, e-skins that can sense and distinguish a variety of static and dynamic pressure stimuli have been successfully implemented.[16–24] In particular, it has been highly desired for the field of intelligent robotics.[25–33] Bao and co-workers recently combined a highly sensitive e-skin exploiting pyramid microstructures arranged along nature-inspired phyllotaxis spirals with a robot arm to provide static pressure feedback while grasping objects.[34] In terms of dynamic pressure detection, Arias' group proposed a single-mode and self-powered mechanoreceptor, which can be applied to a soft-robotic gripper for resolving complex dynamic stimuli.[35] However, the current combination of e-skin and robot merely empowers the feedback of pressure embracing static and dynamic stimuli, which cannot ultimately realize the intelligence of the robot. This often needs establishment of an artificial sensory system to realize the perception and action response to real-life stimulus.[36–39] With the rise of artificial intelligence technology, robots can be facilitated to further possess an advanced perception system so that it can better serve mankind in the aspects of industrial manufacturing, medical health, and social services.[40–46]

Progress and potential

Electronic skin (e-skin) is an electronic device that can simulate the function of human skin to sense external stimuli. With the development of artificial intelligence technology, e-skin is expected to be endowed with the ability to process information so as to help robots have an intelligent perception system and be better applied to people's real life. Here, we report a hybrid e-skin consisting of a piezoresistive pressure sensor and a triboelectric nanogenerator made at low cost and simple preparation methods, which effectively perceives static and dynamic pressure information. Combined with machine-learning technology and an external acquisition circuit, an intelligent material perception system is realized. In addition to monitoring human physiological signals, the hybrid e-skin will open a new avenue for practical intelligent perception and may lead to prominent applications in artificial prostheses, intelligent robots, and human-machine interaction.

Please cite this article in press as: Wei et al., A high-accuracy, real-time, intelligent material perception system with a machine-learning-motivated pressure-sensitive electronic skin, Matter (2022), https://doi.org/10.1016/j.matt.2022.02.016

Toward this end, methods such as machine learning and deep convolutional neural networks can be integrated with the design of e-skin to realize intelligent perception. For instance, Jin et al. demonstrated a smart soft-robotic gripper system composed of patterned-electrode tactile sensors and gear-structured length sensors. By means of machine learning, the soft-robotic gripper system accomplished the identification of different objects and demonstrated its application in virtual assembly lines and smart warehouses.[47] Sundaram et al. proposed a scalable tactile glove based on a tactile sensor array.[48] By relying on the post-processing of tactile information with deep convolutional neural networks, the tactile glove was endowed with smart functions of the recognition of object types and the estimation of object weight. Furthermore, Tee and colleagues realized the rapid recognition and classification of object texture by combining a tactile resistive annularly cracked e-skin with a neural network model for analyzing sensing signals.[49] However, it is still difficult to realize material identification for those objects with indistinguishable appearances such as extremely smooth surfaces. Meanwhile, in an attempt to make robots more closely resemble humans, it is an urgent requirement for an intelligent perception system consisting of the e-skin, signal-acquisition circuit, and artificial neural networks to have the capabilities analogous to the human brain when it interacts with objects, encompassing the real-time acquisition and processing of tactile signals and the ability to distinguish the information obtained from multiple positions simultaneously.

In view of the aforementioned challenges, here we propose a highly sensitive hybrid e-skin in combination with a smart perception system, enabling a tactile perception function superior to human skin in recognizing the material properties of objects with indistinguishably smooth surfaces. The proposed hybrid e-skin, referred to hereafter as PTES, is composed of a flexible piezoresistive pressure sensor (PPS) and a flexible triboelectric nanogenerator (TENG), allowing the high-sensitivity detection of static and dynamic pressure simultaneously. The functional layers of both PPS and TENG are formed by doping natural eggshell membrane (EM) with conductive fillers via a facile infiltration method, giving rise to outstanding virtues of low cost, eco-friendliness, biodegradability, and biocompatibility. Concerning the proposed PPS, we deliberately introduce micro-fence structures in the copper (Cu) electrodes and additionally include a stable thin-film resistor in parallel with a typical PPS, collectively contributing to ultra-high sensitivity. Moreover, the sensitivity can be precisely and linearly adjusted to satisfy diverse application scenarios by readily altering the resistance of the thin-film resistor. In addition to the PTES, we conjointly introduce a field-programmable gate array (FPGA)-based high-speed data collector and multilayer perceptron (MLP) neural network-based machine-learning technique to constitute the material perception system for realizing the real-time sensing of materials with indistinct morphology and smooth surface solely via one touch. Lastly, an array of PTESs with each sensor as a recognition unit is demonstrated to realize the perception of multidimensional information involving multiple material properties and locations, exhibiting a possibility for transcending the human perception system. The proposed PTES in consolidation with the material perception system is not only applied for human physiological information monitoring but also represents a credible new pathway for the realization of robots with intelligent perception and identification of materials featuring an indistinguishable morphology.

RESULTS AND DISCUSSION

Concept and configuration of the proposed e-skin system

Figure 1A shows a schematic illustration of the proposed e-skin system consisting of a hybrid flexible e-skin in conjunction with a material perception system, aiming at simulating and even surpassing the tactile function of biological skin. The hybrid

[1]School of Information Science and Engineering, University of Jinan, Jinan 250022, China

[2]Shandong Provincial Key Laboratory of Network Based Intelligent Computing, University of Jinan, Jinan 250022, China

[3]State Key Laboratory for Superlattices and Microstructures Institute of Semiconductors, University of Chinese Academy of Sciences, Beijing 100083, China

[4]These authors contributed equally

[5]Lead contact

*Correspondence: sunny_lee2011@hotmail.com (Y.L.), gzshen@semi.ac.cn (G.S.)

https://doi.org/10.1016/j.matt.2022.02.016

Please cite this article in press as: Wei et al., A high-accuracy, real-time, intelligent material perception system with a machine-learning-motivated pressure-sensitive electronic skin, Matter (2022), https://doi.org/10.1016/j.matt.2022.02.016

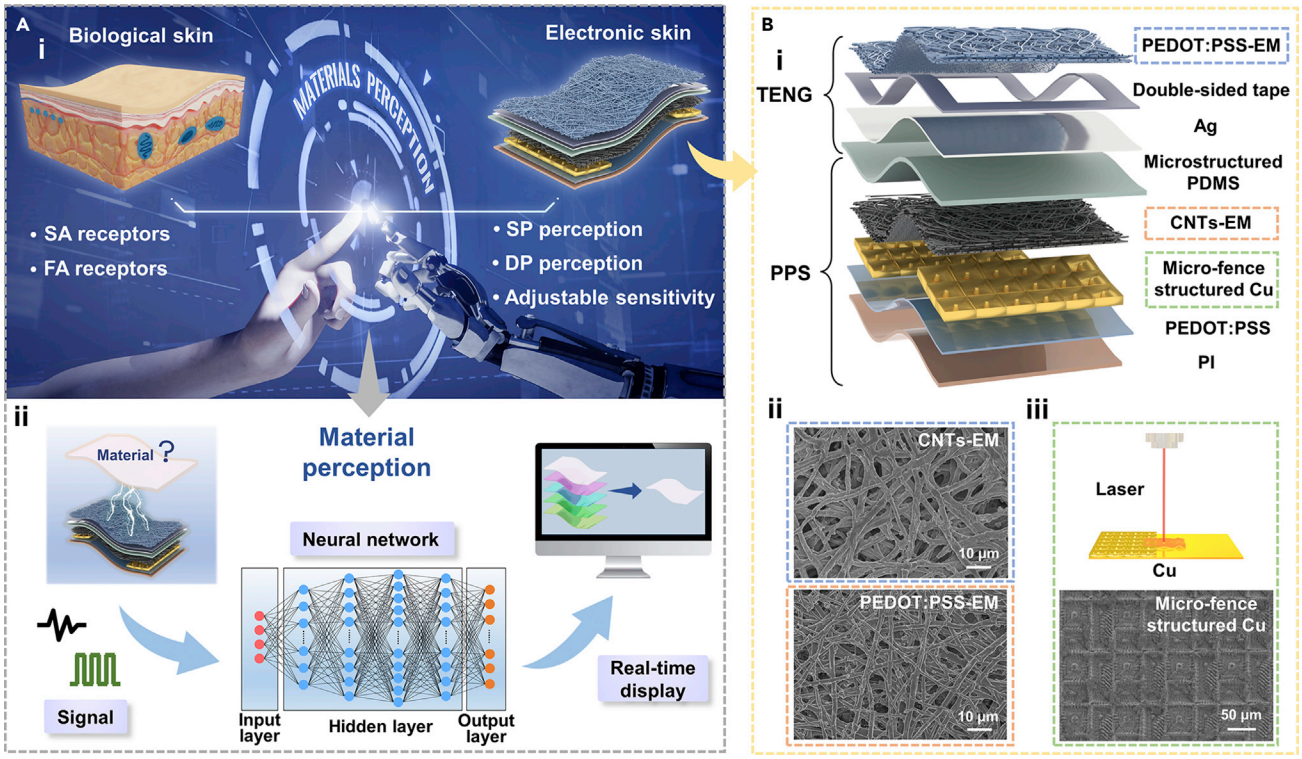

Figure 1. Schematic illustration of the proposed e-skin system

(A) (i) Conceptual diagram of the proposed PTES for material perception. SA receptors and FA receptors represent slow adapting receptors and fast adapting receptors of biological skin, respectively. The proposed PTES has capabilities of simultaneous detection of static pressure (SP) and dynamic pressure (DP) stimuli in combination with adjustable sensitivity to match or even surpass the performances of biological skin. (ii) Schematic overview of the proposed intelligent material perception system, including a signal-acquisition process, a neural network model for signal analysis, and a real-time display interface for presenting the perception result.

(B) (i) Schematic diagram of the PTES composed of a PPS at the bottom and a TENG at the top. (ii) SEM images of the CNTs-EM and PEDOT:PSS-EM functional layers. (iii) Schematic diagram of the micro-fence structures on the Cu electrode prepared by laser marking technology, and SEM image showing the morphology of the micro-fence structured Cu electrode.

e-skin is characterized by two functions of high-sensitivity detection of static and dynamic pressure stimuli and adjustable sensitivity in accordance with distinct applications, by resorting to an integration of a PPS and a TENG, as shown in Figure 1Ai. Figure 1Aii illustrates the proposed material perception system, including a signal (generated when the PTES contacts with the target object) acquisition process, a neural network model (comprising an input layer, four hidden layers, and an output layer) for the recognition of the material properties for different objects, and a real-time display interface for presenting the perception result. Figure 1Bi depicts the structure of the PTES, which contains eight layers from top to bottom (see experimental procedures and Figure S1 for details of the preparation process). Among them, the PPS is mainly composed of a polyimide (PI) tape, a poly(3,4-ethylenedioxythiophene):poly(styrenesulfonate) (PEDOT:PSS) film, micro-fence structured Cu sheets as the electrodes, a carbon nanotubes-eggshell membrane (CNTs-EM) film as the sensing layer, and a microstructured polydimethylsiloxane (PDMS) film, while the TENG primarily consists of three layers including a silver (Ag) film as the electrode, a double-sided tape as the adhesive layer, and a PEDOT:PSS-eggshell membrane (PEDOT:PSS-EM) film as the electrification layer. Considering that EM features porous crossing fibrous structures high specific surface area (Figure S2A) and possesses the property of being easily doped owing to its hydrophilicity, the sensing layer of PPS and the electrification layer of TENG are formed by doping the EM fibers

Please cite this article in press as: Wei et al., A high-accuracy, real-time, intelligent material perception system with a machine-learning-motivated pressure-sensitive electronic skin, Matter (2022), https://doi.org/10.1016/j.matt.2022.02.016

with CNTs and PEDOT:PSS, respectively. The doping process relies only on a low-cost infiltration method. In addition to the simple preparation method, another important reason for selecting CNTs and PEDOT:PSS as conductive fillers to dope EM is their salient merits of superior electrical conductivity, flexibility, biocompatibility, and easy access. Figure 1Bii displays scanning electron microscopy (SEM) images of the prepared CNTs-EM and PEDOT:PSS-EM functional layers, exhibiting a dense arrangement of porous crossing fibrous structures analogous to that of EM. To further confirm the existence of CNTs and PEDOT:PSS, we performed energy-dispersive spectrometry (EDS) to identify that the fibers of EM are evenly and densely wrapped with CNTs and PEDOT:PSS, respectively (Figures S2B–S2F). From the perspective of effectively improving the sensitivity of PPS, we endeavored to introduce the microstructures to the PDMS film and Cu electrodes. For the PDMS film, microstructures (Figure S2G) are formed on one side toward PPS by using sandpaper (Figure S2H), while the other side is kept smooth so as to serve as the substrate for supporting the Ag electrode of the TENG. Laser marking technology is capable of preparing microstructures in a simple, low-cost, shape-controllable, and scale-adjustable manner, thus being a reliable strategy for the fabrication of microstructures of flexible sensors. Therefore, regarding the Cu electrodes, laser marking technology was used to form the micro-fence structures on their surfaces. From the SEM images (Figures 1Biii and S2I), it is apparent that the manufactured micro-fence structures have surface structures similar to the fence-like protrusions and depressions with a uniform and well-defined arrangement. Furthermore, to realize the adjustable sensitivity of PPS, we employed the PEDOT:PSS film to function as a thin-film resistor in parallel with the piezoresistive structure, the resistance of which can be accordingly altered to enable the PPS to possess the desired sensitivity that is linearly adjustable.

PPS characterization and working mechanism

To demonstrate the sensitivity and the pressure response of the proposed PPS (see experimental procedures for details of the measurement method), we performed measurement of the current under various pressure levels with a bias voltage of 1 V. The sensitivity is defined as $S = (\Delta I/I_0)/\Delta P$, where ΔI refers to the current change under the applied pressure, I_0 denotes the initial current without the applied pressure, and ΔP represents the change in the applied pressure. Figure 2A depicts the current as a function of the applied pressure levels, showing a three-stage nearly linear response with unprecedented sensitivity over a wide pressure range. In the middle-pressure range (1.2–12 kPa), the sensitivity is as high as S_2 = 291,699.6 kPa^{-1}. In the low-pressure (0–1.2 kPa) and high-pressure (12–20 kPa) ranges, the sensitivities slightly drop to S_1 = 126,135.9 kPa^{-1} and S_3 = 43,842.1 kPa^{-1}, respectively. Despite this, the minimum sensitivity of the presented sensor here is still higher than the achieved maximum sensitivity of most previously reported similar works. Table S1 lists the performance comparisons between this work and the recently published PPSs. To verify that the obtained ultra-high sensitivity is closely associated with the introduced micro-fence structure in the Cu electrode, we prepared a PPS device with the same structure except for replacing the structured Cu electrode with a plain one as a comparison. From the plot of current varying with applied pressure (Figure S3), one can see that the existence of micro-fence structures within the Cu electrodes greatly increases the pressure sensitivity of our PPS as well as the detection range of pressure. Next, the pressure response and the repeatability of PPS were investigated by alternately loading and unloading pressure onto the sensor for two cycles (Figure 2B). The output current curve under different pressures unveils that the current gradually increases with applied pressure and the current curve remains invariable under the two cycles of loading and unloading pressure, implying superior repeatability. Concerning the current-voltage (*I-V*) curves

Please cite this article in press as: Wei et al., A high-accuracy, real-time, intelligent material perception system with a machine-learning-motivated pressure-sensitive electronic skin, Matter (2022), https://doi.org/10.1016/j.matt.2022.02.016

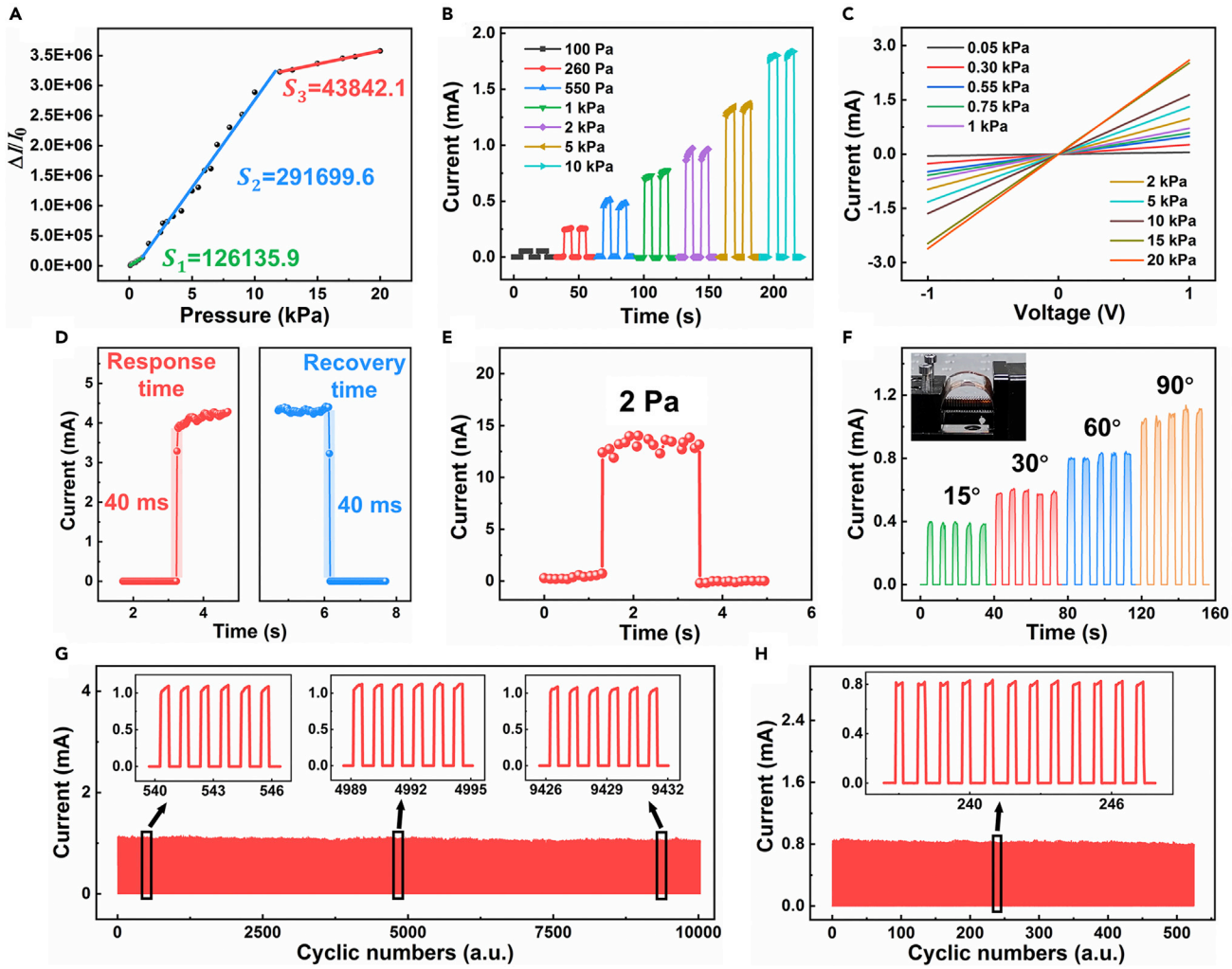

Figure 2. Pressure-sensing performances of the prepared PPS

(A) Pressure response and sensitivity of the PPS under a bias voltage of 1 V. A three-stage linear response with unprecedented sensitivity is obtained over a wide pressure range up to 20 kPa.

(B) Repeatability of the PPS under continuous loading and unloading different pressures ranging from 100 Pa to 10 kPa for two cycles.

(C) Linear relation of the *I-V* curves under different applied pressures, showing that fairly good ohmic contacts are formed between the CNTs-EM sensing layer and micro-fence structured Cu electrodes.

(D) Response and recovery time of PPS under loading and unloading pressure of 21 Pa.

(E) Current response of PPS under minimum detection pressure of 2 Pa.

(F) Plot of current for PPS for different bending angles of 15°, 30°, 60°, and 90°.

(G) Cyclic stability test of the PPS for more than 10,000 cycles. Insets show enlarged views of the marked regions, indicating superior stability.

(H) Cyclic bending test of the PPS over 500 cycles under a fixed angle of 60°. Inset shows enlarged view of the marked region.

of the PPS in the pressure range from 0 to 20 kPa, as presented in Figure 2C, it is clear that a typical linear relation exists and the resistance reduces with increasing applied pressure, indicating that fairly good ohmic contacts are formed between the CNTs-EM and micro-fence structured Cu electrodes.

As the response and recovery time are important factors in characterizing the performance of the sensor, the instant responses of the proposed PPS to both external loading and unloading pressure of 21 Pa were investigated (Figure 2D). Ultrafast response and recovery time of approximately 40 ms was achieved, which allows the PPS to have a response speed comparable with that of human skin (30–50 ms).

Please cite this article in press as: Wei et al., A high-accuracy, real-time, intelligent material perception system with a machine-learning-motivated pressure-sensitive electronic skin, Matter (2022), https://doi.org/10.1016/j.matt.2022.02.016

In addition, the proposed PPS enables a low limit of detection (LOD) of 2 Pa, which is evidenced by the observed noticeable response to pressure in Figure 2E. This allows the designed device to be analogous or even better than the minimum pressure-sensing threshold of human skin (with an LOD of ~100 Pa).[50,51] To evaluate the response capability of the PPS under the bending state, we inspected the changes in current under different bending angles of 15°, 30°, 60°, and 90° over five cycles (Figure 2F). The result indicates that the current increases with enlargement of the bending angle while the responses to the same bending state remain nearly constant. Considering that the sensor is required to be in possession of long-term stability for practical applications, we alternately imposed the loading and unloading pressure of 2.5 kPa onto the PPS for more than 10,000 continuous cycles (Figure 2G). The result of the cyclic test reveals that the demonstrated PPS can rapidly and stably respond to the applied pressure and immediately return to the initial state after unloading the pressure for each cycle, implying remarkable stability and durability of our PPS. The continuous cyclic test in relation to bending was also carried out. The outstanding stability and long-term durability of our PPS are proved by more than 500 cycles of bending/unbending between 0° and 60°, as presented in Figure 2H.

The essential origin underlying the achieved ultra-high sensitivity and long-term durability of the proposed PPS is attributed to an extra conductive path rendered by employing a stable PEDOT:PSS thin-film resistor, which brings about a new degree of freedom to affect the total resistance value of the PPS. Figure 3A illustrates the detailed explanation of the sensing mechanism with the aid of equivalent circuit diagrams. The total resistance of our PPS can be expressed as $R_{total} = R_a // (R_b + (R_{c1} // R_{c2}))$, where R_a is the resistance of the introduced PEDOT:PSS thin-film resistor, R_b is the body resistance of the CNTs-EM sensing layer, R_{c1} refers to the contact resistance between the conducting CNTs-EM layer and the protrusions in the micro-fence structured Cu electrode, and R_{c2} refers to the contact resistance between the conducting CNTs-EM layer and the depressions in the micro-fence structured Cu electrode. In the absence of the imposed pressure to the PPS (initial state), the CNTs-EM sensing layer hardly touches the micro-fence structured Cu electrodes, indicating that the current only flows through the PEDOT:PSS thin-film resistor to form a conductive path (Figure 3Ai). At this point, the total resistance is the initial resistance, equal to the resistance R_a of the PEDOT:PSS thin-film resistor. As the resistance value of the PEDOT:PSS thin-film resistor is unfluctuating, the prepared PPS is thus capable of providing a fairly stable initial resistance (Figure S4). A point worth highlighting is that the selected PEDOT:PSS thin-film resistor has quite a large resistance of $R_a \approx 850\ M\Omega$. When the pressure is applied on the PPS (low-pressure state), the protrusions of the micro-fence structured Cu electrode start to touch the CNTs-EM sensing layer accompanied by the dramatically reduced R_{c1}, resulting in a sum of body resistance and contact resistance $(R_b + R_{c1})$, which is much smaller than the thin-film resistor R_a. A conductive path is thus formed via the upper sensing layer (Figure 3Aii), leading to significantly increased current. Upon further increasing the applied pressure (middle-pressure state), in addition to the protrusions of the micro-fence structured Cu electrodes the irregular structures in the depressions of the Cu electrodes also form effective contacts with the CNTs-EM sensing layer. The contact resistance in this state will reduce to $R_{c1} // R_{c2}$ (Figure 3Aiii), accounting for a relatively larger current. Assuming that we continue to increase the applied pressure (high-pressure state), a complete contact will be formed between the CNTs-EM sensing layer and the Cu electrodes, and the filamentous fibers within the CNTs-EM sensing layer will be compressed, accompanied by the increasing contact points among fibers, giving rise to newly appearing conductive paths (Figure 3Aiv). As a

Please cite this article in press as: Wei et al., A high-accuracy, real-time, intelligent material perception system with a machine-learning-motivated pressure-sensitive electronic skin, Matter (2022), https://doi.org/10.1016/j.matt.2022.02.016

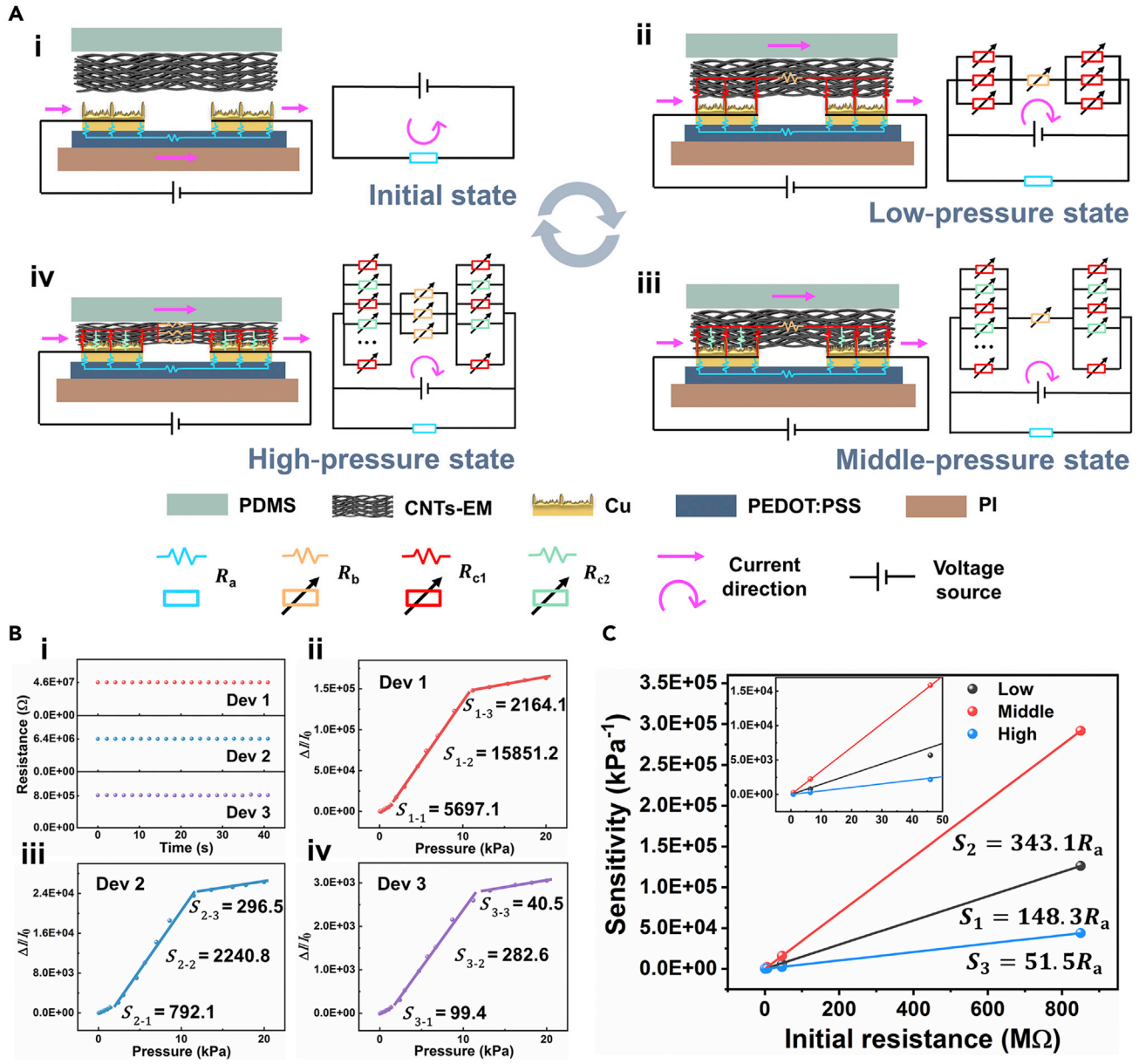

Figure 3. Pressure-sensing mechanism of the PPS and its adjustable sensitivity

(A) Conductive paths formed within the PPS under four different statuses of (i) initial pressure, (ii) low-pressure, (iii) middle-pressure, and (iv) high-pressure states and the corresponding equivalent circuit diagrams.

(B) (i) Prepared samples (Dev1, Dev2, and Dev3) with different initial resistances of 46, 6.4, and 0.8 MΩ. (ii–iv) Sensitivities of three samples in the pressure range of 20 kPa, showing similar three-stage linear pressure-sensing abilities.

(C) Linear relationships between the initial resistances and the sensitivities of all prepared samples including Dev, Dev1, Dev2, and Dev3 in the low-, middle-, and high-pressure ranges. Inset shows enlarged view in the initial resistance range of 0–50 MΩ.

result, the body resistance R_b is decreased, implying that the total resistance R_{total} of the PPS is decreased accordingly.

Based on the above analysis of the sensing mechanism, the total resistance of the proposed PPS rapidly reduces (corresponding to the increasing current) as the applied pressure increases. In addition, the current (denoted as *I*) under the pressure loading is in effect affected by the variations in two resistances, embracing the

Please cite this article in press as: Wei et al., A high-accuracy, real-time, intelligent material perception system with a machine-learning-motivated pressure-sensitive electronic skin, Matter (2022), https://doi.org/10.1016/j.matt.2022.02.016

contact resistance that is dependent on the status between the CNTs-EM sensing layer and micro-fence structured Cu electrodes and the body resistance that is determined by the compression level of the CNTs-EM sensing layer. This is only related to the pressure, and basically independent of the resistance of the adopted thin-film resistor. Therefore, according to $\Delta I = I - I_0$, under the condition that the applied pressure has the same range of variation (ΔP) and I_0 is much smaller than I, the current variation ΔI is approximately constant. Since both the pressure variation ΔP and the current variation ΔI are fixed, high sensitivity can be readily obtained by means of adopting a PEDOT:PSS thin-film resistor with large resistance R_a in correspondence with a tiny initial current I_0. More interestingly, it can be easily deduced that an approximately linear relation exists between the sensitivity S of the proposed PPS and the resistance R_a of the thin-film resistor, alluding that we can precisely acquire the desired sensitivity for the sensor to satisfy distinct scenarios by simply modifying the resistance R_a. As a proof of principle, we prepared three extra samples (denoted Dev1, Dev2, and Dev3) with different initial resistances of 46, 6.4, and 0.8 MΩ by doping the PEDOT:PSS with different proportions of silver nanowires (AgNWs) ethanol solution, as shown in Figure 3Bi. The measured sensitivities of the samples under the applied pressure ranging from 0 to 20 kPa are plotted in Figure 3Bii–iv, where it can be seen that all three samples exhibit three-stage linear pressure responses similar to those in Figure 2A. Surprisingly, the pressure range of each stage is exactly the same as in Figure 2A. To better verify the linear relation between the resistance of the thin-film resistor and pressure sensitivity of the proposed PPS, we plotted the dependence of sensitivity on resistance for all of the samples including the device presented in Figure 2A (denoted as Dev) and the aforementioned samples (Dev1, Dev2, Dev3) in different pressure ranges (low-, middle-, high-pressure ranges) (Figure 3C). It can be intuitively seen that the sensitivity of the prepared sensors linearly varies with the resistance of the thin-film resistor in the low-, middle-, and high-pressure ranges, respectively, in line with our theoretical derivation. The observed linear relations offer us an effective means to predict the sensitivity of the sensor simply by way of straightforwardly measuring the resistance of the thin-film resistor in practice, rather than the commonly used approach that requires the continuous measurement of current under different applied pressures.

TENG characterization and working mechanism

The electrification layer of a TENG plays a vital role in determining the performance of the device. Here, we adopt an EM doped with the conductive filler PEDOT:PSS as the electrification layer of a TENG, as the PEDOT:PSS-EM has high specific surface area and surface charge density, which can effectively increase the contact electrification ability of a TENG. For the purpose of exploring the effect of the concentration of PEDOT:PSS on the electrical output capability of the TENG, three TENGs based on the PEDOT:PSS-EM layer with the different concentrations of PEDOT:PSS (22%, 11%, and 6.6% [v/v]) were prepared. A common PDMS film was used as the counter-friction layer that touches the electrification layers of the prepared TENGs. Figure 4A presents the output voltage as a function of the pressure when the three prepared TENGs contact the surface of the PDMS. Strong voltage responses to the varied pressure are observed for all of the TENGs, of which the one exploiting the electrification layer with the PEDOT:PSS concentrations of 11% (v/v) exhibits a higher output voltage and a more pronounced response to pressure, especially at pressures exceeding 100 kPa. Hence, unless otherwise specified, the following descriptions are based on the TENG with the PEDOT:PSS concentration of 11% (v/v). Figure 4B illustrates the evolution of the output voltage with the pressure continuously increasing from 0.25 to 250 kPa. To further verify the capability of detection of dynamic pressure, we inspected the output voltage of the TENG under the

Please cite this article in press as: Wei et al., A high-accuracy, real-time, intelligent material perception system with a machine-learning-motivated pressure-sensitive electronic skin, Matter (2022), https://doi.org/10.1016/j.matt.2022.02.016

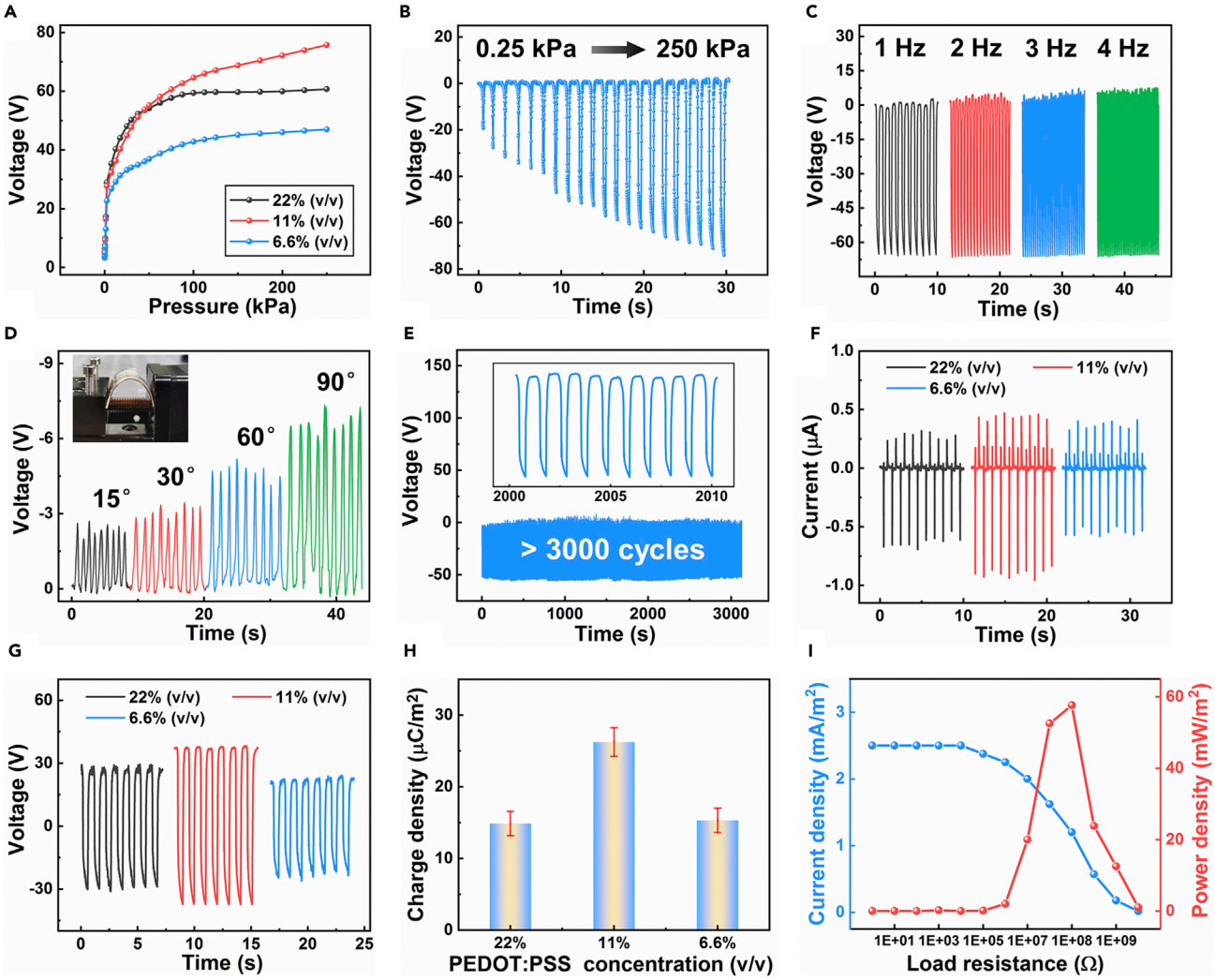

Figure 4. Electrical output performance of the TENG

(A) Output voltage as a function of the applied pressure for three prepared TENGs based on the PEDOT:PSS-EM layer with different PEDOT:PSS concentrations of 22% (v/v), 11% (v/v), and 6.6% (v/v).

(B) Output voltage response of the proposed TENG to the pressure increasing from 0.25 to 250 kPa.

(C) Voltage plot of the TENG for applied pressure of 125 kPa under four different pressing frequencies of 1, 2, 3, and 4 Hz.

(D) Voltage responses of the TENG at different bending angles of 15°, 30°, 60°, and 90°.

(E) Cyclic stability test of the TENG for more than 3,000 cycles. Inset shows magnified view of the voltage plot.

(F–H) (F) Short-circuit current, (G) open-circuit voltage, and (H) charge density of the TENGs based on the electrification layers with different PEDOT:PSS concentrations.

(I) Current density (blue line) and power density (red line) of the proposed TENG under different external load resistances.

frequencies of 1, 2, 3, and 4 Hz for a fixed pressure of 125 kPa, as displayed in Figure 4C, demonstrating that the proposed TENG features an excellent ability to detect dynamic pressure. The slightly increased output voltage with the frequency is ascribed to the accelerated charge accumulation as the frequency increases. Figure 4D shows the output voltage of the TENG under different bending degrees of 15°, 30°, 60°, and 90°, indicating that the bending angle can be evidently and readily recognized according to the output voltage. In addition, the output voltage of the TENG can be stably maintained for more than 3,000 continuous cycles of alternately loading and unloading the pressure, implying favorable durability and repeatability enabled by the proposed TENG, as presented in Figure 4E. Through the above

Please cite this article in press as: Wei et al., A high-accuracy, real-time, intelligent material perception system with a machine-learning-motivated pressure-sensitive electronic skin, Matter (2022), https://doi.org/10.1016/j.matt.2022.02.016

analysis, the proposed TENG sensor is verified to feature a prominent and stable sensing capability that can be applied to detect the dynamic pressure and bending angle.

Moreover, as a nanogenerator, the proposed TENG also features a self-powering capability. To evaluate this fundamental capability, we conducted short-circuit current and open-circuit voltage tests at a frequency of 1 Hz. The test results (Figures 4F and 4G) reveal that the TENG that is likewise based on the PEDOT:PSS concentration of 11% (v/v) demonstrates the best performance. The measured maximum short-circuit current and open-circuit voltage are 0.9 μA and 78 V, respectively. In the light of the measured charge density (Figure 4H), the TENG with the PEDOT:PSS concentration of 11% (v/v) offers the highest charge density of approximately 26.3 $\mu C/m^2$. The changing trend of the current and power densities under the variation of load resistance for a fixed frequency of 1 Hz is displayed in Figure 4I, indicating that the current density continuously decreases with increasing value of load resistance, while a maximum power density of 58 mW/m^2 is obtained when the load resistance is 100 MΩ. Through a bridge rectifier circuit, the output pulse voltage of the TENG can be applied to charge a commercial capacitor. As shown in Figure S5, a 1 μF capacitor is rapidly charged to 2 V within 8 s. Similarly, a "UJN" icon composed of 23 light-emitting diodes in series can be simultaneously lit up via continuous pressing of the TENG (Figure S6). The demonstrated ability to drive small electronic devices advocates the proposed TENG to have great potential in the field of self-powered wearable electronic devices. The working mechanism of the proposed TENG is based on the coupling effect of contact electrification and electrostatic induction between PEDOT:PSS-EM and PDMS.[52–55] When the PEDOT:PSS-EM and PDMS layers are in contact, the different abilities of the two layers to capture charges induce the electron transfer. In the separation process, electrostatic induction causes the movement of free electrons on the electrode. By continuously repeating the process of contact and separation between PDMS and PEDOT:PSS-EM, electrical signals can be continuously generated. The detailed working mechanism is scrutinized in Note S1 and Figure S7.

Applications of PTES for static and dynamic pressure sensing

Based on the above investigation, it is confirmed that the separate PPS and TENG can enable the sensing of static and dynamic pressure via the measurement of current and voltage, respectively. A complete PTES based on the integration of the PPS with the TENG was prepared and inspected. In terms of the static pressure detection, we utilized the PTES to perform a human pulse-monitoring test, which is deemed to be a key application of e-skin in human health monitoring because the pulse is an important physiological signal that reflects the physical condition of the human body and is closely related to many diseases. Figure 5A plots the monitored pulse information under two situations, before (normal) and after exercise, by fixing the prepared PTES on a fingertip of a 25-year-old adult male. It is clearly seen that the pulse waveform before exercise is characterized by a frequency of about 66 times per minute and each pulse has three distinct peaks of percussion wave (P_1), tidal wave (P_2), and diastolic wave (P_3), corresponding to systolic/diastolic blood pressure, ventricular pressure, and heart rate, respectively,[56,57] as shown in the enlarged image on the right. After exercise, the beating frequency of the fingertip pulse is accelerated to 96 beats per minute and the beating intensity is conspicuously enhanced. In the light of the magnified image marked by a dotted box, it is observed that the pulse waveform after exercise alters greatly as the peak P_2 disappears. The disappearance of peak P_2 is predominantly attributed to the change of the heart or ventricular pump.[58] In addition to the fingertip pulse monitoring, other

Please cite this article in press as: Wei et al., A high-accuracy, real-time, intelligent material perception system with a machine-learning-motivated pressure-sensitive electronic skin, Matter (2022), https://doi.org/10.1016/j.matt.2022.02.016

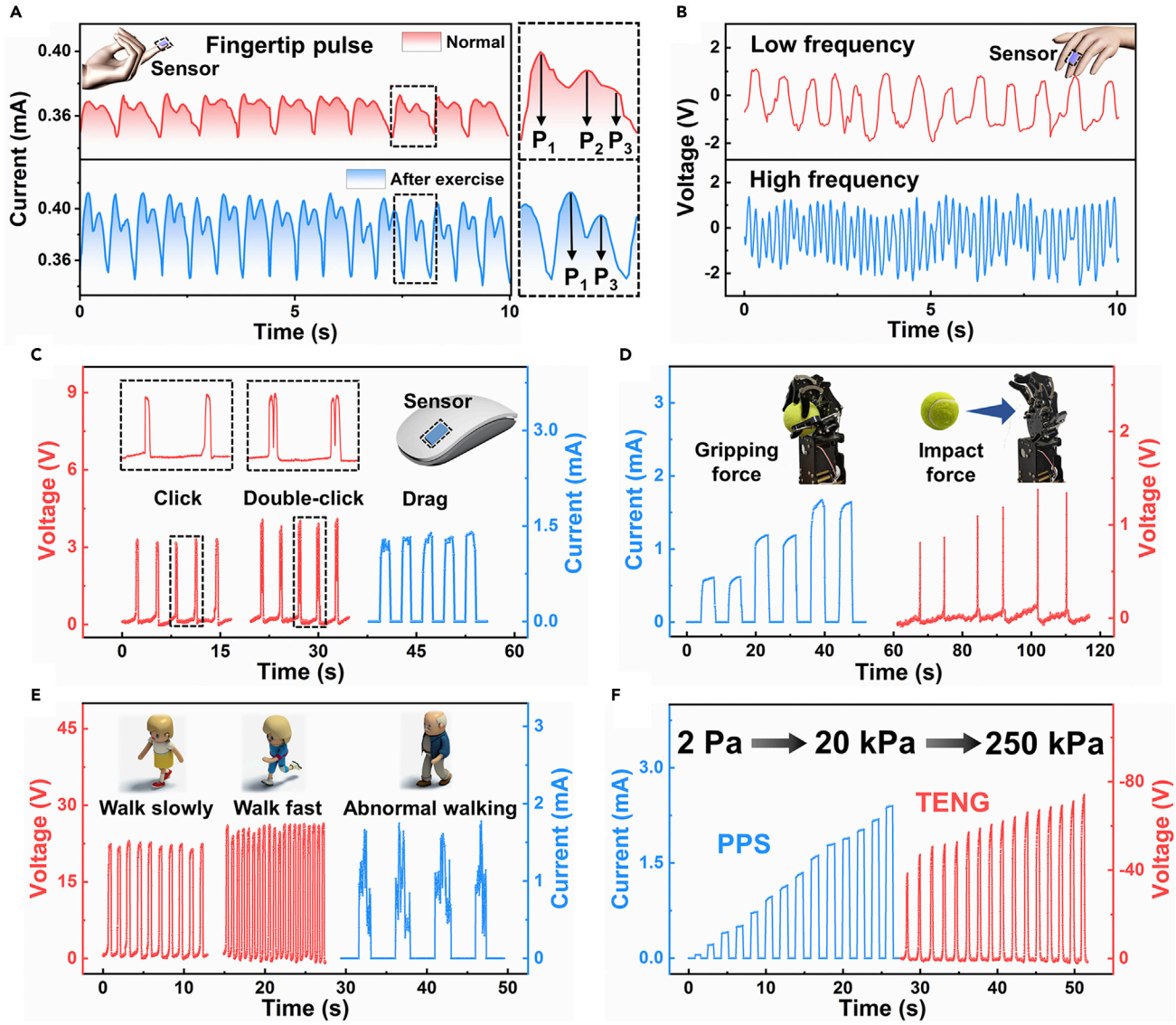

Figure 5. Applications of PTES for static and dynamic pressure sensing

(A) Fingertip pulse signals before and after exercise by attaching the PTES to the fingertip. Insets on the right are enlarged views of the marked regions in the diagram on the left.

(B) Finger tremor signals under the low and high frequencies.

(C) Voltage and current signals corresponding to the mouse under different actions of click, double-click, and drag. Insets show magnified views of the marked regions.

(D) Current and voltage signals in relation to the manipulator gripping the ball with different forces (gripping force) and the ball impinging on the manipulator at different speeds (impact force), respectively.

(E) Current and voltage signals pertaining to the different walking status including slow, fast, and abnormal walking by fixing the PTES to the soles of the feet.

(F) Current and voltage responses to different applied pressures over an extremely wide range of 2–250 kPa.

human physiological signals including radial artery, carotid artery, and heartbeat pulses before and after exercise were also inspected by placing the PTES on the wrist, the neck, and the chest near the heart, respectively (Figures S8A–S8C). Finger tremor (seen as dynamic pressure) is another signal that can reflect the health of the human body, as it usually appears in situations of mental stress, emotional agitation, extreme physical fatigue, and even in relation to some diseases such as Parkinson's syndrome. By fixing the proposed PTES on the finger and measuring the output

Please cite this article in press as: Wei et al., A high-accuracy, real-time, intelligent material perception system with a machine-learning-motivated pressure-sensitive electronic skin, Matter (2022), https://doi.org/10.1016/j.matt.2022.02.016

voltage, the tremor information of the finger at low and high frequencies can be accurately monitored, as shown in Figure 5B. The accurate monitoring of human pulse signals and finger tremors indicates that the proposed PTES can afford the detection of static and dynamic pressures with high sensitivity and can be applied to monitor human physiological signals.

To demonstrate that the proposed PTES has the ability to detect dynamic pressure as well as static pressure simultaneously, we fixed the PTES to a mouse and checked its response to a mouse click, double-click, and drag action, respectively (Figure 5C). With regard to the mouse click and the double-click (seen as dynamic pressure), distinct peaks can be clearly observed in the voltage curves during each click. Especially for the double-click, two consecutive voltage peaks can be apparently distinguished, which is confirmed by the zoomed-in view of the region marked by a dotted black box. For the drag action of the mouse (seen as static pressure), we measured the current curve under the mouse drag state whereby a strong response was clearly observed. In addition, by simply sticking the PTES to the touch control switch of a desk lamp, we verified that the proposed PTES can accurately capture the signals of turning on (touch the lamp switch), brightening (touch the lamp switch again), and turning off the lamp (long-press the lamp switch), respectively (Figure S9). For a more practical application, we combined the PTES with a manipulator to enable the manipulator to sense the grasping force in real time while grasping objects. The current curve in Figure 5D (denoted by a blue line) shows the perception of the gripping forces by the PTES placed on the palm of the manipulator when the manipulator continuously grips a ball with three different forces at small, medium, and large levels. It is seen that the sensing response features different intensities, which primarily corresponds to the magnitude of the applied static pressure. Apart from the detection of the static gripping force, it is also necessary to be able to detect the instantaneous impact force that emerges when the ball touches the palm of the manipulator. Here, we consider the situations that the ball touches the palm of the manipulator at three different speeds, which correspond to different magnitudes of the dynamic impact forces. It can be observed from Figure 5D (denoted by a red line) that the output voltage response is proportional to the magnitude of impact force. Hence, the manipulator is verified to be capable of monitoring the static gripping force and dynamic impact force simultaneously by placing the proposed PTES upon it. In addition, the monitoring of human walking status, embracing slow walking, fast walking, and abnormal walking, can be realized by placing the PTES on the soles of the feet (Figure 5E). As the contact time between the foot and the ground is relatively short when a normal person walks slowly or quickly, the output voltage is measured to detect these two statuses, as shown by the red line in Figure 5E. One can see that both the frequency and the amplitude of the output voltage in the fast walking state are higher than those in the slow walking state, which is consistent with the actual situation. Given that for people with leg disabilities the contact time between the foot and the ground is long and the force is uneven during walking, the current curve is thus measured to monitor this state, as plotted by the blue line in Figure 5E. The measured current waveform superbly reflects the state of uneven force during walking. According to the aforementioned experiments, the proposed PTES is proved to exhibit great potential in fields of human physiological information monitoring, manipulator tactile sensation, and monitoring of human walking status. Another intriguing observation is that the proposed PTES can offer a fairly broad pressure range from 2 Pa to 250 kPa by means of integrating the TENG with the PPS to compensate the performance degradation of PPS under high-pressure states (Figure 5F). Specifically, with regard to the detection of the applied pressure less than 20 kPa, the current signal generated by the PPS

Please cite this article in press as: Wei et al., A high-accuracy, real-time, intelligent material perception system with a machine-learning-motivated pressure-sensitive electronic skin, Matter (2022), https://doi.org/10.1016/j.matt.2022.02.016

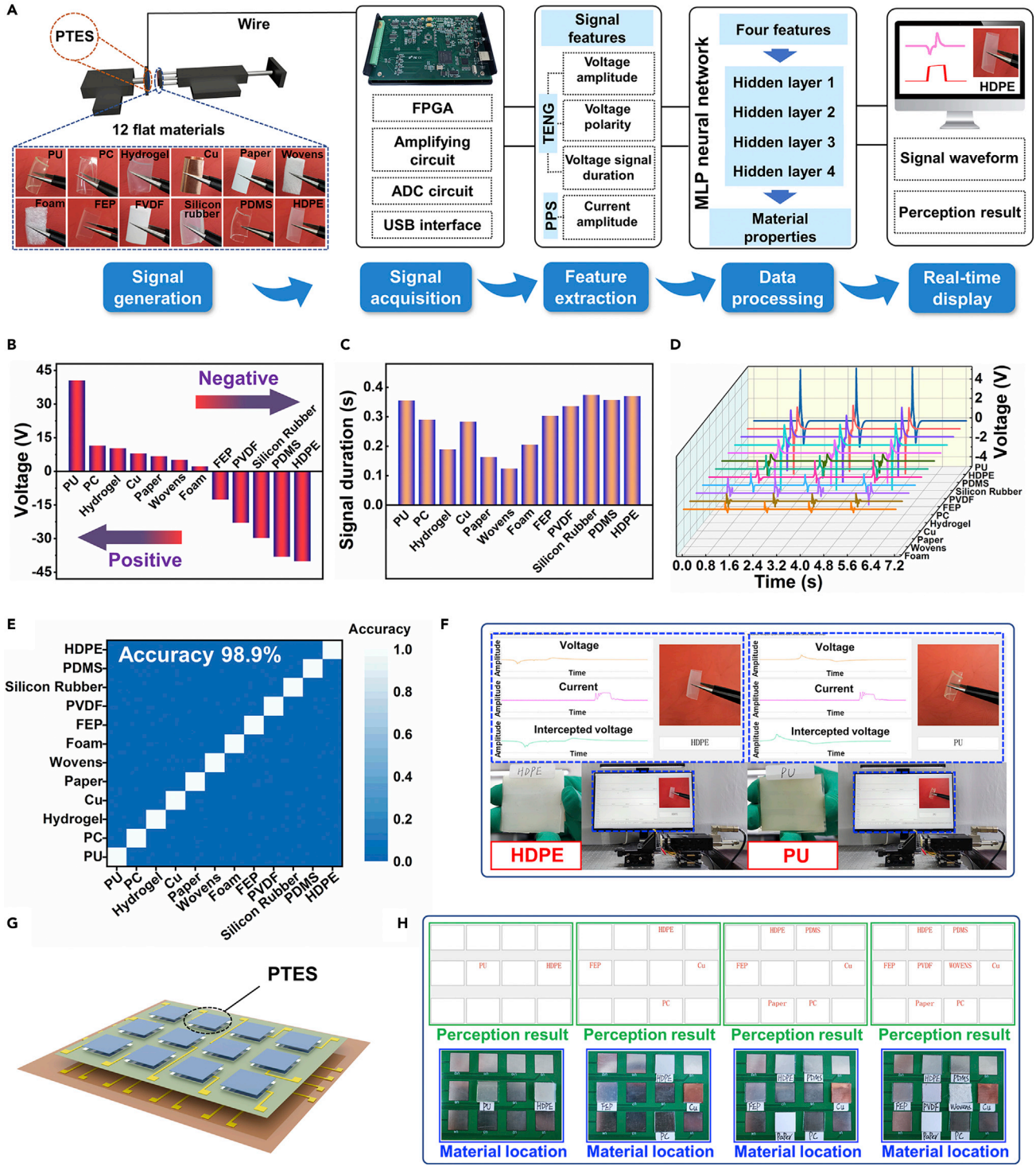

Figure 6. Machine-learning-assisted intelligent material perception system

(A) Schematic overview of the established material perception system, which consists of a self-built setup for signal generation, an FPGA-based high-speed data collector for signal acquisition, a feature-extraction module for extracting four features of the signals, an MLP model for data processing and analysis, and a display interface for showing perception results in real time.

(B) Output voltage amplitudes and polarities of the PTES in contact with 12 kinds of materials.

(C) Output voltage signal durations of the PTES in contact with 12 kinds of materials.

(D) Voltage signal waveforms acquired by the FPGA-based high-speed data collector when the PTES contacts 12 kinds of materials.

Please cite this article in press as: Wei et al., A high-accuracy, real-time, intelligent material perception system with a machine-learning-motivated pressure-sensitive electronic skin, Matter (2022), https://doi.org/10.1016/j.matt.2022.02.016

Figure 6. *Continued*

(E) Accuracy of recognition of 12 materials by using the trained MLP model.

(F) Real-time display of the perception results for HDPE and PU by using the constructed material perception system.

(G) Schematic illustration of an array of PTESs containing 3 × 4 perception units.

(H) Simultaneous display of the perception results for 2, 4, 6, and 8 materials, located in different positions on a plate, by relying on the prepared PTES array in combination with the proposed material perception system.

part is preferentially monitored. When the applied pressure exceeds 20 kPa, the sensing of pressure chiefly depends on the monitoring of the output voltage signal from the TENG part.

Machine-learning-assisted material perception system

To enable interaction with the real world, the PTES is supposed to have the ability to infer the material property of the object with which it is in contact, similar to human skin. It is worth noting that it is quite challenging for the human skin to identify the material property of an object featuring a smooth surface with indistinguishable characteristics. By means of integrating the proposed PTES with an MLP neural network-assisted intelligent material perception system, we were able to identify the material property in real time when touching objects with smooth surfaces, exhibiting a distinguished capability beyond the perception of human skin. The established intelligent material perception system is schematically illustrated in Figure 6A, including generation and acquisition of signals, feature extraction, data processing and analysis, and real-time display of results. Twelve kinds of flat materials with smooth and indistinguishable surfaces that cannot be directly identified by human hands are selected as representative test materials. The PTES sample and tested materials are respectively attached to a fixed stage and a movable stage that can move back and forth via a linear motor. Meanwhile, the linear motor can control the applied pressure as well. With regard to the signal that needs to be acquired, the voltage signal is given priority of consideration, as the TENG of PTES would generate complicated voltage signals featuring different amplitudes, polarity, and signal durations when different materials are in contact with the PEDOT:PSS-EM layer of PTES. The reason underlying the generated distinct voltage signal is chiefly attributed to the coupling effect of contact electrification and electrostatic induction, which is affected by the intrinsic properties of contact materials including electron affinity, work function, and friction.[59] As a proof of concept, we performed an output voltage test under a given pressure of 20 kPa for each of 12 kinds of flat materials when in contact with PTES. It is worth noting that the selected test materials are characterized by extremely smooth surfaces and cannot be directly identified by human hands. As depicted in Figure 6B, seven materials including polyurethane (PU), polycarbonate (PC), hydrogel, Cu, paper, wovens, and foam exhibit strong tribo-positive behavior compared with the PEDOT:PSS-EM layer, thus indicating that positive output voltages have been detected. On the contrary, the remaining five materials including fluorinated ethylene propylene (FEP), poly(vinylidene fluoride) (PVDF), silicon rubber, PDMS, and high-density polyethylene (HDPE) show strong tribo-negative behavior, giving rise to negative voltages. The tribo-positive or tribo-negative behaviors observed from the material exclusively depend on the inherent abilities of material to lose or gain electrons upon contact with other materials.[60–62] The amplitudes of output voltages are observed to be unique for each material under consistently applied pressure, as intended. Similar to the voltage amplitude, the signal duration for each material also shows unique value, as shown in Figure 6C. Nevertheless, once the same material contacts the PTES with different pressures (ranging from 0.25 to 20 kPa), the amplitude and signal duration of the output voltage closely follows the variations in applied pressure and only the polarity of contact status retains the same, which can be confirmed

Please cite this article in press as: Wei et al., A high-accuracy, real-time, intelligent material perception system with a machine-learning-motivated pressure-sensitive electronic skin, Matter (2022), https://doi.org/10.1016/j.matt.2022.02.016

by Figures S10 and S11. The changes in the voltage amplitude and signal duration are deemed to originate from the fact that the altered pressure induces changes in the parameters of friction, effective contact area, and viscosity coefficient between the TENG and the detected material.[63,64] The polarity of contact status is invariable because it merely depends on the inherent ability of a material to lose or gain electrons upon contact with another material, as previously mentioned. Based on the above discussions, it turns out that the result is insufficient to accurately identify the material by solely monitoring the output voltage signal. To eliminate the impact of the pressure variations, we monitored the current signal extracted from the PPS of PTES simultaneously to sense the applied pressure. Since each material corresponds to a unique voltage response when it comes into contact with the PTES under the same pressure, as long as the applied pressure is known, the type of material can be recognized via the unique voltage response.

In the signal-acquisition process, a vital point is the undistorted acquisition of the output voltage waveform in real time as the voltage waveform is characterized by instantaneously sharp pulses. Here, an FPGA-based high-speed data collector integrating an amplifying circuit, an analog-to-digital converter (ADC) circuit, and a universal serial bus (USB) interface was expressly adopted to precisely acquire the output voltage waveforms. The acquired voltage waveforms in relation to different materials, as depicted in Figure 6D, exhibit distinct features in terms of voltage amplitude, signal duration, and polarity of contact status (see Table S2 for detailed data). Here, the amplitude of the collected voltage signal is proportionally reduced because several resistors in series have been used to divide the voltage during the signal collection owing to the limited range of the high-speed data collector. Thereafter, to enable the PTES to acquire material perception ability, we performed an MLP model training process based on a dataset formed by 23,223 sets of data in relation to the acquired signals corresponding to 12 materials. Each set of data contains four features including the amplitude, signal duration, and polarity of contact status extracted from the voltage waveform, and the amplitude of the current waveform. It is worth noting that the samples in the dataset are diversified, including the data collected at multiple time points and under various environments, so as to avoid the impact of environmental factors on the accuracy of material recognition. Ultimately the recognition accuracy after training can reach up to 98.9%, as plotted in Figure 6E. Table S3 summarizes the recognition accuracy of each material with the trained MLP model. Taking the perception of HDPE and PU as examples, the perception results, as well as the acquired voltage and current waveforms, can be precisely displayed on the terminal computer screen in real time through only one touch, as shown in Figure 6F and Video S1. Figure S12 and Video S1 present the perception results of the remaining ten materials. Taking the influence of the variation in the applied pressure on the perception result into consideration, Figure S13 further displays the perception results in real time when the applied pressure of the HDPE in contact with the PTES is altered. Hence, it is confirmed that the constructed intelligent material perception system is capable of real-time identification and display of the material property of the object when in contact with the PTES via one touch at arbitrary pressure.

To mimic the ability of human skin to simultaneously identify multiple objects located in different regions through one touch, we prepared a sensor array comprising 3 × 4 PTESs, each of which behaves as a material perception unit (Figure 6G). For the purpose of eliminating the signal crosstalk between neighboring PTESs when acquiring multiple signals at the same time, we designed a power amplifier circuit to augment the signals (see the circuit diagram in Figure S14). Similar to

Please cite this article in press as: Wei et al., A high-accuracy, real-time, intelligent material perception system with a machine-learning-motivated pressure-sensitive electronic skin, Matter (2022), https://doi.org/10.1016/j.matt.2022.02.016

the PTES array, a plate with the same dimension was prepared on which to place the test materials. The plate is divided into 12 regions, each of which corresponds to the region in which the PTES unit is located in the array. We respectively placed 2, 4, 6, and 8 kinds of materials in random positions on the plate, as shown in the bottom row of Figure 6H. When the plate on which the materials are placed is in contact with the prepared PTES array, the PTES units in the position where the material is placed perceive the corresponding materials and generate voltage and current signals in their respective channels. By inputting the acquired signals into the trained MLP neural network model, the type of materials and their positions on the plate can be recognized, respectively, as displayed in the top row of Figure 6H. The acquired voltage and current signals in real time are shown in Figure S15. The entire material recognition process can be viewed in detail in Video S2. Our results verify that the prepared PTES array has the capability of simultaneously perceiving multiple materials through only one contact of each unit and that the perception results can be displayed on the computer in real time. The demonstrated intelligent material perception system based on the combination of the proposed hybrid e-skin (PTES) and the MLP neural network is proposed to harbor tremendous practical application value and potential in the field of robotic tactile perception.

Conclusions

In this work, a high-sensitivity and low-cost hybrid e-skin embracing two sensors of PPS and TENG is proposed and demonstrated to realize real-time perception of multiple materials. The functional layers of PPS and TENG are formed by adopting cost-effective and eco-friendly EMs in combination with a facile infiltration method. To improve the sensing performance of PPS, we made adjustments in terms of two aspects of structure design, namely manufacturing micro-fence structures on the Cu electrodes by means of laser marking technology and adding a PEDOT:PSS thin-film resistor in parallel with the typical piezoresistive structure. It has been proved that the demonstrated PPS endows a maximum sensitivity reaching 291,699.6 kPa^{-1} and outstanding long-term durability. With the aid of an extra conducting path offered by an introduced thin-film resistor, the PPS has been proved to have stable initial resistance and to enable a linearly adjustable sensitivity by changing the resistance value of the thin film. As the most significant highlight of this work, we further demonstrated a material perception system by applying an FPGA-based high-speed data collector and an MLP neural network model to collect and analyze the static and dynamic tactile sensing information provided by PTES. The system is able to recognize 12 materials with indistinguishable surfaces via one touch, with an accuracy of 98.9%, and the perception results can be displayed in real time. Lastly, a 3 × 4 PTES array was developed to illustrate its application potential in the simultaneous perception of multiple objects with respect to their material properties and locations, successfully demonstrating its outstanding capability to process multiple information. It can be anticipated that the proposed hybrid e-skin design architecture, preparation method, sensitivity-adjustable modeling method, and intelligent material perception system will pave the way to realize smart robots with extraordinary perception ability and bring new inspiration to the fields of self-powered wireless wearable systems, human-machine interactions, and intelligent prostheses.

EXPERIMENTAL PROCEDURES

Resource availability

Lead contact

Further information and requests for resources and materials should be directed to and will be fulfilled by the lead contact, Guozhen Shen (gzshen@semi.ac.cn).

Please cite this article in press as: Wei et al., A high-accuracy, real-time, intelligent material perception system with a machine-learning-motivated pressure-sensitive electronic skin, Matter (2022), https://doi.org/10.1016/j.matt.2022.02.016

Materials availability

This study did not generate new unique reagents.

Data and code availability

The data used to support the findings of this study are available from the lead contact upon reasonable request.

Preparation of PEDOT:PSS-EM and CNTs-EM composite films

The preparation process of PEDOT:PSS-EM and CNTs-EM composite films are depicted in Figure S1A. At first, the EM was manually peeled from an eggshell of fresh egg. The peeled EM was cleaned three times in deionized water, then completely dried on a hot plate at 50°C, eventually giving rise to the desired EM featuring a double-sided fibrous structure. Next, 10 mL of PEDOT:PSS conductive ink (EL-P3040; AGFA, Belgium) was dissolved in 20 mL of 95% ethanol, followed by sonicating for 1 h until it was completely dissolved. The resulting solution was centrifuged at 12,000 rpm for 6 min to remove sediment. The supernatant was collected and mixed in deionized water at different volume ratios (1:0.5, 1:2, 1:4) to prepare the PEDOT:PSS solution with different concentrations of 22%, 11%, and 6.6% (v/v), which are recorded as solutions A, B, and C, respectively. Subsequently, the pretreated EMs were immersed in solutions A, B, and C for 6 h and completely dried to obtain the EMs modified by the PEDOT:PSS with different concentrations (PEDOT:PSS-EMs). For the CNTs-EM, 10 mg of carbon nanotubes (length of 10–30 μm, XFNANO, China) and 100 mg of SDS (AR ≧99.0%, Shanghai Macklin Biochemical, China) were dissolved in 20 mL of deionized water and sonicated for 4 h until the CNTs were completely dispersed. Thereafter, the pretreated EM was immersed in the CNT dispersions and sonicated for 1 h, followed by drying for 3 h to obtain the CNTs-modified EM (CNTs-EM).

Preparation of Cu electrode with micro-fence structure

The uniform micro-fence pattern on the Cu tape-based electrode was realized by using an UV laser marking machine (FM-UVM3; Fermi, China) with marking parameters including 20% power, frequency 5 kHz, and speed 200 mm/s.

Preparation of microstructured PDMS-Ag multilayer

The preparation process of the microstructured PDMS-Ag layer is shown in Figure S1B. First, the base and curing agent of PDMS (Sylgard 184; Dow Corning, USA) were mixed in a ratio of 10:1 (w/w) and fully stirred, followed by vacuum degassing for 1 h. The prepared PDMS was spin-coated on commercial sandpaper (roughness of #2400) at a rotation speed of 400 rpm and dried in an oven at 80°C for 2 h. After oxygen plasma treatment (65 W, 30 s), Ag was deposited on the PDMS-coated sandpaper by a magnetron sputtering method. Finally, the sandpaper was manually removed so that the desired layers with the microstructured PDMS on one side and the Ag conductive layer on the opposite side were obtained.

Preparation of PEDOT:PSS thin-film resistors with different resistance values

Figure S1C displays the preparation process of the PEDOT:PSS thin-film resistors. A PI tape was initially treated by oxygen plasma (45 W, 30 s), and a PEDOT:PSS (1.5% in water, Aladdin Industrial, China) film was coated on the PI tape, followed by drying at 50°C for 2 h. By mixing 2 mL of PEDOT:PSS (1.5% in water, Aladdin Industrial) with 0.3, 0.6, and 1 mL of AgNW ethanol solutions (average length 20 μm, XFNANO), three mixtures were prepared and coated, respectively on the PI tapes via the same method mentioned above. Eventually, four PEDOT:PSS thin-film resistors with resistance values of about 850, 46, 6.4, and 0.8 MΩ were prepared.

Please cite this article in press as: Wei et al., A high-accuracy, real-time, intelligent material perception system with a machine-learning-motivated pressure-sensitive electronic skin, Matter (2022), https://doi.org/10.1016/j.matt.2022.02.016

Assembly of the PTES

Two prepared micro-fence structured Cu electrodes were attached on both sides of the PEDOT:PSS film, and the CNTs-EM sensing layer was sandwiched between the Cu electrodes and microstructured PDMS-Ag. It is worth noting that the side of the Cu electrodes with the micro-fence structures and the side of the PDMS with the microstructures were both set to face the CNTs-EM. Finally, the prepared PEDOT:PSS-EM was attached to the Ag electrode belonging to the PDMS-Ag multilayer by using a double-sided adhesive tape, resulting in the complete PTES.

Fabrication of the PTES array

A flat plate composed of 12 small squares (1 × 1 cm for each square) was designed for placement of the PTES units, each of which was located in the center of the small square. Hence, a 3 × 4 PTES array was formed. To avoid the signal crosstalk between PTES units, each PTES was designed to possess independent electrodes.

Characterization and measurements

The observation of SEM images and the EDS analysis were carried out by using a field emission scanning electron microscope (Regulus-8100; Hitachi, Japan). A linear motor (PS01; LinMot, Switzerland) was used to supply the applied pressure. An electrometer (6517B; Keithley, USA) was used to measure the short-circuit current, open-circuit voltage, and transfer charges of the TENG. It is worth mentioning that the TENG operates in single-electrode mode and the Ag conductive layer of TENG was connected to the electrometer during the measurement for the dynamic response (Figure S16). The output current signal of the PPS was measured by using a digital source meter (2602B; Keithley). Here, two micro-fence structured Cu electrodes of PPS were connected to the digital source meter via conductive tapes to measure the current in correspondence with the static response (Figure S16).

Signal acquisition and communication

The voltage and current signals were acquired using a self-built high-speed data collector, which primarily exploited FPGA integrated with amplifier circuit, 12-bit ADC circuit, and USB interface. The FPGA-based high-speed data collector was equipped with 8-channel ports and 4 kHz of single-channel sampling rate. With FPGA functioning as the main control module, the voltage and current analog signals generated by the PTES were amplified via the amplifier circuit and then entered the ADC circuit to realize the conversion of continuous analog signals into discrete digital signals. Finally, the acquired digital signals were delivered to the computer for subsequent extraction of signal features via the USB interface.

Training and optimization of MLP neural network model

An MLP neural network model was implemented in the TensorFlow framework to process and analyze the acquired signals for the PTES to realize material perception. The MLP model consists of an input layer, four fully connected hidden layers, and an output layer. There are four neurons in the input layer that correspond to the four features (voltage amplitude, voltage signal duration, voltage polarity of contact status, and current amplitude) extracted from the acquired voltage (TENG) and current (PPS) signals , and 12 neurons in the output layer that represent the output recognition probabilities of the 12 materials using the SoftMax activation function. In respect of the hidden layers, the number of neurons for each layer was set as 12, 32, 256, and 64, respectively, and rectified linear units activation functions were introduced to all of the layers. The Adam optimizer was adopted to optimize the MLP model, in which the learning rate of the model is set to 0.1, and the categorical cross-entropy loss function was used to evaluate the differences between the

predicted probability distributions after training and the true distribution. Lastly, we used the training dataset to train the MLP model for 400 epochs with batches of 32 data samples.

SUPPLEMENTAL INFORMATION

Supplemental information can be found online at https://doi.org/10.1016/j.matt.2022.02.016.

ACKNOWLEDGMENTS

This work was supported by the National Natural Science Foundation of China under grants 62174068, 61805101, 62005095, 61888102, and 61625404; Shandong Provincial Natural Science Foundation of China under grants ZR2019BF013 and ZR2020QF105; and Rizhao City Key Research and Development Program under grant 2021ZDYF010102.

AUTHOR CONTRIBUTIONS

Y.L. and G.S. conceived this work. X.W., Y.L., and H.L. designed, prepared, and tested the hybrid e-skin. X.W. and H.L. developed the overall intelligent material perception system and verified the feasibility of this architecture. W.Y., S.G., and Y.L. helped with the experimental design and preparation of the material perception system. Y.L., W.Y., H.L., Z.C., and X.W. participated in the discussion of experimental results. W.Y., X.W., S.G., and Y.L. wrote the manuscript. G.S. and Y.L. supervised the project. All authors reviewed and commented on the manuscript.

DECLARATION OF INTERESTS

The authors declare no competing interests.

Received: November 26, 2021
Revised: January 27, 2022
Accepted: February 14, 2022
Published: March 15, 2022

REFERENCES

1. Meng, K., Zhao, S., Zhou, Y., Wu, Y., Zhang, S., He, Q., Wang, X., Zhou, Z., Fan, W., Tan, X., et al. (2020). A wireless textile-based sensor system for self-powered personalized health care. Matter *2*, 896–907.

2. Jinno, H., Yokota, T., Koizumi, M., Yukita, W., Saito, M., Osaka, I., Fukuda, K., and Someya, T. (2021). Self-powered ultraflexible photonic skin for continuous bio-signal detection via air-operation-stable polymer light-emitting diodes. Nat. Commun. *12*, 2234.

3. Fang, Y., Zou, Y., Xu, J., Chen, G., Zhou, Y., Deng, W., Zhao, X., Roustaei, M., Hsiai, T.K., and Chen, J. (2021). Ambulatory cardiovascular monitoring via a machine-learning-assisted textile triboelectric sensor. Adv. Mater. *33*, 2104178.

4. Niu, S., Matsuhisa, N., Beker, L., Li, J., Wang, S., Wang, J., Jiang, Y., Yan, X., Yun, Y., Burnett, W., et al. (2019). A wireless body area sensor network based on stretchable passive tags. Nat. Electron. *2*, 361–368.

5. Liu, H., Zhang, S., Li, Z., Lu, T.J., Lin, H., Zhu, Y., Ahadian, S., Emaminejad, S., Dokmeci, M.R., Xu, F., et al. (2021). Harnessing the wide-range strain sensitivity of bilayered PEDOT:PSS films for wearable health monitoring. Matter *4*, 1–16.

6. Yu, X., Xie, Z., Yu, Y., Lee, J., Vazquez-Guardado, A., Luan, H., Ruban, J., Ning, X., Akhtar, A., Li, D., et al. (2019). Skin-integrated wireless haptic interfaces for virtual and augmented reality. Nature *575*, 473–479.

7. Li, W., Li, C., Zhang, G., Li, L., Huang, K., Gong, X., Zhang, C., Zheng, A., Tang, Y., Wang, Z., et al. (2021). Molecular ferroelectric-based flexible sensors exhibiting supersensitivity and multimodal capability for detection. Adv. Mater. *33*, 2104107.

8. Zhao, X., Zhang, Z., Liao, Q., Xun, X., Gao, F., Xu, L., Kang, Z., and Zhang, Y. (2020). Self-powered user-interactive electronic skin for programmable touch operation platform. Sci. Adv. *6*, eaba4294.

9. Kim, Y., Chortos, A., Xu, W., Liu, Y., Oh, J.Y., Son, D., Kang, J., Foudeh, A.M., Zhu, C., Lee, Y., et al. (2018). A bioinspired flexible organic artificial afferent nerve. Science *360*, 998–1003.

10. Yang, J.C., Mun, J., Kwon, S.Y., Park, S., Bao, Z., and Park, S. (2019). Electronic skin: recent progress and future prospects for skin-attachable devices for health monitoring, robotics, and prosthetics. Adv. Mater. *31*, 1904765.

11. Sim, K., Rao, Z., Zou, Z., Ershad, F., Lei, J., Thukral, A., Chen, J., Huang, Q.-A., Xiao, J., and Yu, C. (2019). Metal oxide semiconductor nanomembrane–based soft unnoticeable multifunctional electronics for wearable human-machine interfaces. Sci. Adv. *5*, eaav9653.

12. Moin, A., Zhou, A., Rahimi, A., Menon, A., Benatti, S., Alexandrov, G., Tamakloe, S., Ting, J., Yamamoto, N., Khan, Y., et al. (2021). A wearable biosensing system with in-sensor adaptive machine learning for hand gesture recognition. Nat. Electron. *4*, 54–63.

13. Yin, R., Wang, D., Zhao, S., Lou, Z., and Shen, G. (2020). Wearable sensors-enabled human-machine interaction systems: from design to application. Adv. Funct. Mater. *31*, 2008936.

14. Wang, S., Xu, J., Wang, W., Wang, G.-J.N., Rastak, R., Molina-Lopez, F., Chung, J.W., Niu, S., Feig, V.R., Lopez, J., et al. (2018). Skin electronics from scalable fabrication of an intrinsically stretchable transistor array. Nature *555*, 83–88.

15. Yao, S., Ren, P., Song, R., Liu, Y., Huang, Q., Dong, J., O'Connor, B.T., and Zhu, Y. (2019). Nanomaterial-enabled flexible and stretchable sensing systems: processing, integration, and applications. Adv. Mater. *32*, 1902343.

16. Bai, N., Wang, L., Wang, Q., Deng, J., Wang, Y., Lu, P., Huang, J., Li, G., Zhang, Y., Yang, J., et al. (2020). Graded intrafillable architecture-based iontronic pressure sensor with ultra-broad-range high sensitivity. Nat. Commun. *11*, 209.

17. Guo, H., Tan, Y.J., Chen, G., Wang, Z., Susanto, G.J., See, H.H., Yang, Z., Lim, Z.W., Yang, L., and Tee, B.C.K. (2020). Artificially innervated self-healing foams as synthetic piezo-impedance sensor skins. Nat. Commun. *11*, 5747.

18. Gao, Y., Yu, L., Yeo, J.C., and Lim, C.T. (2019). Flexible hybrid sensors for health monitoring: materials and mechanisms to render wearability. Adv. Mater. *32*, 1902133.

19. Wang, Y., Wu, H., Xu, L., Zhang, H., Yang, Y., and Wang, Z.L. (2020). Hierarchically patterned self-powered sensors for multifunctional tactile sensing. Sci. Adv. *6*, eabb9083.

20. Ji, B., Zhou, Q., Hu, B., Zhong, J., Zhou, J., and Zhou, B. (2021). Bio-inspired hybrid dielectric for capacitive and triboelectric tactile sensors with high sensitivity and ultrawide linearity range. Adv. Mater. *33*, 2100859.

21. Hua, Q., Sun, J., Liu, H., Bao, R., Yu, R., Zhai, J., Pan, C., and Wang, Z.L. (2018). Skin-inspired highly stretchable and conformable matrix networks for multifunctional sensing. Nat. Commun. *9*, 244.

22. Chun, S., Son, W., Kim, H., Lim, S.K., Pang, C., and Choi, C. (2019). Self-powered pressure- and vibration-sensitive tactile sensors for learning technique-based neural finger skin. Nano Lett. *19*, 3305–3312.

23. Shi, L., Li, Z., Chen, M., Qin, Y., Jiang, Y., and Wu, L. (2020). Quantum effect-based flexible and transparent pressure sensors with ultrahigh sensitivity and sensing density. Nat. Commun. *11*, 3529.

24. Dong, K., Wu, Z., Deng, J., Wang, A.C., Zou, H., Chen, C., Hu, D., Gu, B., Sun, B., and Wang, Z.L. (2018). A stretchable yarn embedded triboelectric nanogenerator as electronic skin for biomechanical energy harvesting and multifunctional pressure sensing. Adv. Mater. *30*, 1804944.

25. Shen, Z., Zhu, X., Majidi, C., and Gu, G. (2021). Cutaneous ionogel mechanoreceptors for soft machines, physiological sensing, and amputee prostheses. Adv. Mater. *33*, 2102069.

26. Han, M., Wang, H., Yang, Y., Liang, C., Bai, W., Yan, Z., Li, H., Xue, Y., Wang, X., Akar, B., et al. (2019). Three-dimensional piezoelectric polymer microsystems for vibrational energy harvesting, robotic interfaces and biomedical implants. Nat. Electron. *2*, 26–35.

27. Chun, S., Kim, J.-S., Yoo, Y., Choi, Y., Jung, S.J., Jang, D., Lee, G., Song, K.-I., Nam, K.S., Youn, I., et al. (2021). An artificial neural tactile sensing system. Nat. Electron. *4*, 429–438.

28. Yang, W., Gong, W., Gu, W., Liu, Z., Hou, C., Li, Y., Zhang, Q., and Wang, H. (2021). Self-powered interactive fiber electronics with visual-digital synergies. Adv. Mater. *33*, 2104681.

29. Osborn, L.E., Dragomir, A., Betthauser, J.L., Hunt, C.L., Nguyen, H.H., Kaliki, R.R., and Thakor, N.V. (2018). Prosthesis with neuromorphic multilayered e-dermis perceives touch and pain. Sci. Robot. *3*, eaat3818.

30. Guo, Y., Wei, X., Gao, S., Yue, W., Li, Y., and Shen, G. (2021). Recent advances in carbon material-based multifunctional sensors and their applications in electronic skin systems. Adv. Funct. Mater. *31*, 2104288.

31. Justus, K.B., Hellebrekers, T., Lewis, D.D., Wood, A., Ingham, C., Majidi, C., LeDuc, P.R., and Tan, C. (2019). A biosensing soft robot: autonomous parsing of chemical signals through integrated organic and inorganic interfaces. Sci. Robot. *4*, eaax0765.

32. Ren, Y., Liu, Z., Jin, G., Yang, M., Shao, Y., Li, W., Wu, Y., Liu, L., and Yan, F. (2021). Electric-field-induced gradient ionogels for highly sensitive, broad-range-response, and freeze/heat-resistant ionic fingers. Adv. Mater. *33*, 2008486.

33. Byun, J., Lee, Y., Yoon, J., Lee, B., Oh, E., Chung, S., Lee, T., Cho, K.-J., Kim, J., and Hong, Y. (2018). Electronic skins for soft, compact, reversible assembly of wirelessly activated fully soft robots. Sci. Robot. *3*, eaas9020.

34. Boutry, C.M., Negre, M., Jorda, M., Vardoulis, O., Chortos, A., Khatib, O., and Bao, Z. (2018). A hierarchically patterned, bioinspired e-skin able to detect the direction of applied pressure for robotics. Sci. Robot. *3*, eaau6914.

35. Wu, X., Zhu, J., Evans, J.W., and Arias, A.C. (2020). A single-mode, self-adapting, and self-powered mechanoreceptor based on a potentiometric-triboelectric hybridized sensing mechanism for resolving complex stimuli. Adv. Mater. *32*, 2005970.

36. Wen, F., Zhang, Z., He, T., and Lee, C. (2021). AI enabled sign language recognition and VR space bidirectional communication using triboelectric smart glove. Nat. Commun. *12*, 5378.

37. Wang, M., Luo, Y., Wang, T., Wan, C., Pan, L., Pan, S., He, K., Neo, A., and Chen, X. (2021). Artificial skin perception. Adv. Mater. *33*, 2003014.

38. Zhang, X., Zhuo, Y., Luo, Q., Wu, Z., Midya, R., Wang, Z., Song, W., Wang, R., Upadhyay, N.K., Fang, Y., et al. (2020). An artificial spiking afferent nerve based on Mott memristors for neurorobotics. Nat. Commun. *11*, 51.

39. Rahman, M.A., Walia, S., Naznee, S., Taha, M., Nirantar, S., Rahman, F., Bhaskaran, M., and Sriram, S. (2020). Artificial somatosensors: feedback receptors for electronic skins. Adv. Intell. Syst. *2*, 2000094.

40. Li, G., Liu, S., Wang, L., and Zhu, R. (2020). Skin-inspired quadruple tactile sensors integrated on a robot hand enable object recognition. Sci. Robot. *5*, eabc8134.

41. Mahler, J., Matl, M., Satish, V., Danielczuk, M., DeRose, B., McKinley, S., and Goldberg, K. (2019). Learning ambidextrous robot grasping policies. Sci. Robot. *4*, eaau4984.

42. Zhu, M., Sun, Z., Zhang, Z., Shi, Q., He, T., Liu, H., Chen, T., and Lee, C. (2020). Haptic-feedback smart glove as a creative human-machine interface (HMI) for virtual/augmented reality applications. Sci. Adv. *6*, eaaz8693.

43. Tan, H., Tao, Q., Pande, I., Majumdar, S., Liu, F., Zhou, Y., Persson, P.O.Å., Rosen, J., and Dijken, S.v. (2020). Tactile sensory coding and learning with bioinspired optoelectronic spiking afferent nerves. Nat. Commun. *11*, 1369.

44. Shih, B., Shah, D., Li, J., Thuruthel, T.G., Park, Y.-L., Iida, F., Bao, Z., Kramer-Bottiglio, R., and Tolley, M.T. (2020). Electronic skins and machine learning for intelligent soft robots. Sci. Robot. *5*, eaaz9239.

45. Kadumudi, F.B., Hasany, M., Pierchala, M.K., Jahanshahi, M., Taebnia, N., Mehrali, M., Mitu, C.F., Shahbazi, M.A., Zsurzsan, T.G., Knott, A., et al. (2021). The manufacture of unbreakable bionics via multifunctional and self-healing silk-graphene hydrogels. Adv. Mater. *33*, 2100047.

46. Kim, K.K., Ha, I., Kim, M., Choi, J., Won, P., Jo, S., and Ko, S.H. (2020). A deep-learned skin sensor decoding the epicentral human motions. Nat. Commun. *11*, 2149.

47. Jin, T., Sun, Z., Li, L., Zhang, Q., Zhu, M., Zhang, Z., Yuan, G., Chen, T., Tian, Y., Hou, X., et al. (2020). Triboelectric nanogenerator sensors for soft robotics aiming at digital twin applications. Nat. Commun. *11*, 5381.

48. Sundaram, S., Kellnhofer, P., Li, Y., Zhu, J.-Y., Torralba, A., and Matusik, W. (2019). Learning the signatures of the human grasp using a scalable tactile glove. Nature *569*, 698–702.

49. Yao, H., Yang, W., Cheng, W., Tan, Y.J., See, H.H., Li, S., Ali, H.P.A., Lim, B.Z., Liu, Z., and Tee, B.C.K. (2020). Near-hysteresis-free soft tactile electronic skins for wearables and reliable machine learning. Proc. Natl. Acad. Sci. U.S.A. *117*, 25352–25359.

50. Zhu, P., Du, H., Hou, X., Lu, P., Wang, L., Huang, J., Bai, N., Wu, Z., Fang, N.X., and Guo, C.F. (2021). Skin-electrode iontronic interface for mechanosensing. Nat. Commun. *12*, 4731.

51. Johansson, R.S., and Flanagan, J.R. (2009). Coding and use of tactile signals from the fingertips in object manipulation tasks. Nat. Rev. Neurosci. *10*, 345–359.

52. Zhou, K., Zhao, Y., Sun, X., Yuan, Z., Zheng, G., Dai, K., Mi, L., Pan, C., Liu, C., and Shen, C. (2020). Ultra-stretchable triboelectric nanogenerator as high-sensitive and self-powered electronic skins for energy harvesting and tactile sensing. Nano Energy *70*, 104546.

53. Lai, Y.-C., Deng, J., Liu, R., Hsiao, Y.-C., Zhang, S.L., Peng, W., Wu, H.-M., Wang, X., and Wang, Z.L. (2018). Actively perceiving and responsive soft robots enabled by self-powered, highly extensible, and highly sensitive triboelectric proximity- and pressure-sensing skins. Adv. Mater. *30*, 1801114.

54. Chen, S.W., Cao, X., Wang, N., Ma, L., Zhu, H.R., Willander, M., Jie, Y., and Wang, Z.L. (2016). An ultrathin flexible single-electrode triboelectric-nanogenerator for mechanical

energy harvesting and instantaneous force sensing. Adv. Energy Mater. *7*, 1601255.

55. Wang, Z.L., Chen, J., and Lin, L. (2015). Progress in triboelectric nanogenerators as a new energy technology and self-powered sensors. Energy Environ. Sci. *8*, 2250–2282.

56. Wang, X., Gu, Y., Xiong, Z., Cui, Z., and Zhang, T. (2014). Silk-molded flexible, ultrasensitive, and highly stable electronic skin for monitoring human physiological signals. Adv. Mater. *26*, 1336–1342.

57. O'Rourke, M.F. (1971). The arterial pulse in health and disease. Am. Heart J. *82*, 687–702.

58. Chen, S., Zhuo, B., and Guo, X. (2016). Large area one-step facile processing of microstructured elastomeric dielectric film for high sensitivity and durable sensing over wide pressure range. ACS Appl. Mater. Inter. *8*, 20364–20370.

59. Liu, Z., Li, H., Shi, B., Fan, Y., Wang, Z.L., and Li, Z. (2019). Wearable and implantable triboelectric nanogenerators. Adv. Funct. Mater. *29*, 1808820.

60. Khandelwal, G., Maria Joseph Raj, N.P., and Kim, S.-J. (2021). Materials beyond conventional triboelectric series for fabrication and applications of triboelectric nanogenerators. Adv. Energy Mater. *11*, 2101170.

61. Mathew, A.A., Chandrasekhar, A., and Vivekanandan, S. (2020). A review on real-time implantable and wearable health monitoring sensors based on triboelectric nanogenerator approach. Nano Energy *80*, 105566.

62. Wang, Z.L. (2013). Triboelectric nanogenerators as new energy technology for self-powered systems and as active mechanical and chemical sensors. ACS Nano *7*, 9533–9557.

63. Nurmakanov, Y., Kalimuldina, G., Nauryzbayev, G., Adair, D., and Bakenov, Z. (2021). Structural and chemical modifications towards high-performance of triboelectric nanogenerators. Nanoscale Res. Lett. *16*, 122.

64. Hu, G., Zhao, C., Yang, Y., Li, X., and Liang, J. (2022). Triboelectric energy harvesting using an origami-inspired structure. Appl. Energy *306*, 118037.